Engineering Structures 196 (2019) 109328

Contents lists available at ScienceDirect

Engineering Structures

journal homepage: www.elsevier.com/locate/engstruct

Low cycle fatigue performance investigation on Transverse Steel Dampers for bridges under ground motion sequences using shake-table tests

Lianxu Zhou[a], Xiaowei Wang[a,b], Aijun Ye[a,*]

[a] State Key Laboratory of Disaster Reduction in Civil Engineering, Tongji University, 1239 Siping Rd., Shanghai 200092, China
[b] College of Civil and Transportation Engineering, Hohai University, 1 Xikang Rd., Nanjing 210024, China

ARTICLE INFO

Keywords:
Low cycle fatigue
Transverse steel damper
Shake-table test
Ground motion sequence

ABSTRACT

The low cycle fatigue performance of metallic hysteretic dampers is widely concerned by researchers because the energy-dissipation mechanism of these dampers primarily relies on inelastic deformations of metals. To examine the low cycle fatigue performance of a metallic hysteretic damper for bridges, called the Transverse Steel Damper (TSD), shake-table tests are conducted on a 1/35-scaled cable-stayed bridge model installed with two types of TSDs with different yield strengths, and the bridge model is subjected to a series of ground motion sequences including pulse- and non-pulse-like ground motions. After that, the post-earthquake capacities of TSDs are further examined using monotonic quasi-static tests and compared with their pre-earthquake capacities. Then, three theoretical methods in the literature, two of which are improved in this study, are used to assess the fatigue performance of TSDs. The results indicate an excellent low cycle fatigue performance for TSDs, which experienced more than ten strong shakings and almost remained the original performance without any fatigue failure.

1. Introduction

In the last few decades, the concept of structural damage control has attracted wide attention from both academic and engineering communities. The goal of this concept is to limit the earthquake-induced damages to specific components such as energy dissipation dampers for the purpose of protecting super- and sub-structures. Under this background, a large number of damping devices especially passive dampers, including viscous dampers, viscoelastic dampers, friction dampers, and metallic hysteretic dampers, etc., have been widely used in bridge engineering and structure engineering [1–4] due to their easy constructions and convenient implementations. Among these passive dampers, the metallic hysteretic dampers that dissipate seismic energy through inelastic deformations of metals have been proved to be superior in economy, durability, and reliability and so forth [5–7]. Since Kelly et al. [8] put forward the concept of energy absorption using metallic dampers in 1972, a variety of metallic hysteretic dampers were proposed and studied by researchers through experiments and/or numerical simulations. According to the yielding mechanism, these hysteretic dampers can be generally categorized into four types, including the bending-type such as steel plate/bar energy dissipation devices [9–13], the axial compression-tension type such as Buckling Restrained Braces (BRBs) [14], the shear-type such as Shear Panel Dampers (SPDs) [15] and the torsion-type such as torsional beam et al. [16]. Recently, Shen et al. [17] developed a bending-type device called Transverse Steel Damper (TSD), which adopts triangular steel-plates as energy-dissipation components, for the transverse seismic mitigation of cable stayed bridges. The TSDs can freely accommodate the longitudinal movement of bridge decks under service condition loads. This unique property distinguishes TSDs from existing bending-type devices. The authors have performed a series of quasi-static and shake-table tests and associated numerical analyses to verify the excellent dissipation capacity of TSDs [17,18]. A noted limitation in the previous studies is the lack of experimental verification on the low cycle fatigue performance of TSDs, which provides the motivation of the current study.

Since the energy dissipation mechanism of metallic hysteretic dampers primarily relies on inelastic deformations of metals, their low cycle fatigue issues have been concerned by many researchers [19–23]. In particular, multiple strong aftershocks may occur shortly after a destructive main shock [24]. For example, the 2015 Nepal earthquake witnessed seven sequential strong motions (moment magnitude, $M_w > 5.3$) near Gorkha from April 25 to 27 [25]. Also, in the 2016 Kumamoto earthquake, three strong shakings ($M_w > 6$) occurred in Kyushu Island within only three days [26,27]. Therefore, dampers in bridges located in these seismic-prone areas may experience multiple excitations during their service lives. Under such frequently sequential

* Corresponding author.
E-mail addresses: csuzlx@tongji.edu.cn (L. Zhou), x.wang@hhu.edu.cn (X. Wang), yeaijun@tongji.edu.cn (A. Ye).

https://doi.org/10.1016/j.engstruct.2019.109328
Received 3 February 2019; Received in revised form 21 May 2019; Accepted 20 June 2019
Available online 28 June 2019

shakings, in general, there is no opportunity to repair or replace those impaired dampers in gaps of these shakings. Therefore, an excellent and reliable low cycle fatigue performance should be possessed by metallic hysteretic dampers.

There are a few requirements for the low cycle fatigue performance of metallic hysteretic dampers in various seismic design specifications. For example, the American Institute of Steel Construction (AISC) stipulates that BRBs should sustain cumulative inelastic axial deformations at least 200 times of their yield deformations [28]. In Chinese specification [29], an index called Equivalent Hysteretic Cycles (EHCs), which should not be less than **30**, is used to assess the low cycle fatigue performance of metallic dampers. Aside from these stipulations, some notable research has focused on the low cycle fatigue issues of metallic hysteretic dampers in recent years [14,30–32]. For example, Usami et al. [14,23] and Wang et al. [32] investigated the low cycle fatigue performance of BRBs under variable and constant strain amplitudes using quasi-static tests, and they pointed that the BRBs installed in structures should withstand strong earthquakes three times without replacements. In their studies, an index named Cumulative Inelastic Deformation (CID) was adopted to assess the low cycle fatigue performance of BRBs, and 0.7 is recommended as the ultimate value of CID for BRBs. Xu et al. [33] investigated the low cycle fatigue performance of low-yield-point SPDs using reversed cyclic loading quasi-static tests. Camara et al. [34] theoretically evaluated the low cycle fatigue performance of a bending-type device using a strain-based method. In short, existing studies mainly focus on the low cycle fatigue performance of axial compression-tension-type (e.g., BRBs) and shear-type (e.g., SPDs) metallic hysteretic dampers using quasi-static load-patterns, while relatively few experimental studies focus on the low cycle fatigue performance of bending-type metallic hysteretic dampers such as TSDs. Moreover, the real scenario of dampers experiencing ground motions can be better reproduced by shake-table tests. Therefore, it is a better way to assess low cycle fatigue performance than conventional quasi-static tests.

This paper aims to examine the low cycle fatigue performance of TSDs using shake-table tests. Two sets of TSDs with different yield-strengths are separately installed on a 1/35-scaled cable-stayed bridge model, which is subjected to ground motion sequences in the Multi-functional Shaking Table Lab at Tongji University, Shanghai, China. After that, the post-earthquake capacities of the tested TSDs are assessed using monotonic quasi-static tests. Then, the abovementioned three theoretical methods, including the strain-based, the CID-based and the EHC-based methods, together with assistance of numerical simulations, are adopted to assess the low cycle fatigue performance of TSDs.

2. Test program

2.1. Descriptions of shake-table tests and TSDs

A 1/35-scale model of the Sutong Bridge (a cable-stayed bridge with a main span of 1088 m) was designed. Fig. 1 schematically shows the layout of the shake-table test and configurations of deck-bent and –tower connections. As shown in Fig. 1(a), the total length of the test model is 59.66 m, and the height of towers is 8.58 m. Four shake-tables (A to D) are used in the test. Bents 1 and 2 are mounted on Table A, and Tower 1 is mounted on Table B. Fig. 1(b) and (c) shows deck-bent/tower connections. As shown in these figures, TSDs are placed at deck-bent and -tower connections in the bridge model as energy dissipation device, and the layout of TSDs is as follows: one TSD is placed at each deck-bent connection in parallel with two sliding spherical steel bearings, while two TSDs are installed at each deck-tower connection. Note that for the purpose of conciseness, only key information of the shake-table test is introduced here, while other detailed information can be found in [18].

Fig. 2 presents the full view of the test model and the detailed deck-bent/tower connections. Since the deformation of TSD at Bent 2 is slightly larger than those at Tower 1 and Bent 1 under the selected seismic inputs (presented in Section 2.3), the TSD located at Bent 2 is selected as the main research object. Detailed configurations of the deck-Bent 2 connection and measurements are illustrated in Figs. 1(b) and Fig. 2(c). The displacement of TSD was measured by a string potentiometer. Additionally, tri-axial-force sensors were placed at bottoms of the TSD to measure horizontal forces transferred from deck to bents and towers.

Fig. 3 presents the detailed configuration of the tested TSD, namely, one TSD consists of two parallel triangle-steel-plates, each with a width of 7 cm, a height of 11 cm and a thickness of 0.3 cm. To examine the low cycle fatigue performance of TSDs with different yield strengths, two sets of TSDs (named TSD-1 and TSD-2) are installed separately on the bridge model. Note that the triangle-steel-plates in the TSD-1 and TSD-2 have identical geometric dimensions, while different yield strengths (i.e., 326 and 193 MPa for TSD-1 and TSD-2, respectively). Table 1 lists the geometric parameters and configuration of the tested TSDs.

2.2. Properties of TSDs

To obtain mechanical parameters of the studied TSDs, including yield-strength, pre- and post-yield stiffness, three samples of TSD-1 and three samples of TSD-2 are randomly selected to carry out quasi-static tests. Theoretically, the two parallel plates in a TSD move synchronously under horizontal loads [17]. Therefore, only one triangular steel plate was tested for simplicity, and the lateral force of one TSD is twice as large as that of one plate. As schematically shown in Fig. 4, a simplified monotonic loading device is designed which is composed of the iron shelf, pulley, steel wire, weights, and pallet. The load is transferred to the TSD through the steel wire across the pulley. The horizontal displacement at the plate top is monitored by a string potentiometer. In addition, strains at different locations of the triangular plate bottom were also recorded to validate the ABAQUS numerical model for TSD, which will be introduced in Section 4.1.3.

Regarding the loading protocol of the monotonic loading, a 3 kg pallet is loaded to TSD at first, followed by the load increment of 4.85 kg. The test is completed when the recorded horizontal displacement of TSD reaches its design displacement. In this paper, the design displacement of TSD-1 and TSD-2 is 4.7 cm, which is determined by two principles as described in [17]. One is to retain the integrity of the TSD, namely preventing the hemispheres from jumping out of the steel blocks (refer to Fig. 3). The other is that strains at the bottom of the triangular steel plate corresponding to the design displacement should be less than its ultimate strain.

Fig. 5 shows global force-displacement curves of TSD-1 and TSD-2. The dotted lines represent the measured results from the quasi-static tests. The equivalent bilinear force-displacement relationship of the TSD can then be estimated by the records. The mechanical parameters of TSD-1 and TSD-2 are listed in Table 2.

2.3. Ground motions and loading scheme

To examine the low cycle fatigue performance of TSDs under different ground motions, four ground motions are selected from the PEER-NGA ground motion database [35], including the far-field ground motions (#1, San Fernando and #2, El Centro), the near-fault non-pulse-like one (#3, Chi-Chi) and the near-fault pulse-like one (#4, Landers). Table 3 lists the information of these records, including stations, record sequence number (RSN), average shear wave velocity at top 30 m of the site (V_{s30}), magnitude (M_w) and source distance (R). Fig. 6 indicatively displays the time-compressed ground motions scaled to the same Peak Ground Acceleration (PGA) (i.e., 0.5 g). Note that the scale-factor for durations of ground motions is 0.169 determined by the similarity design of the test model [18].

Fig. 7 illustrates acceleration spectra of these time-compressed

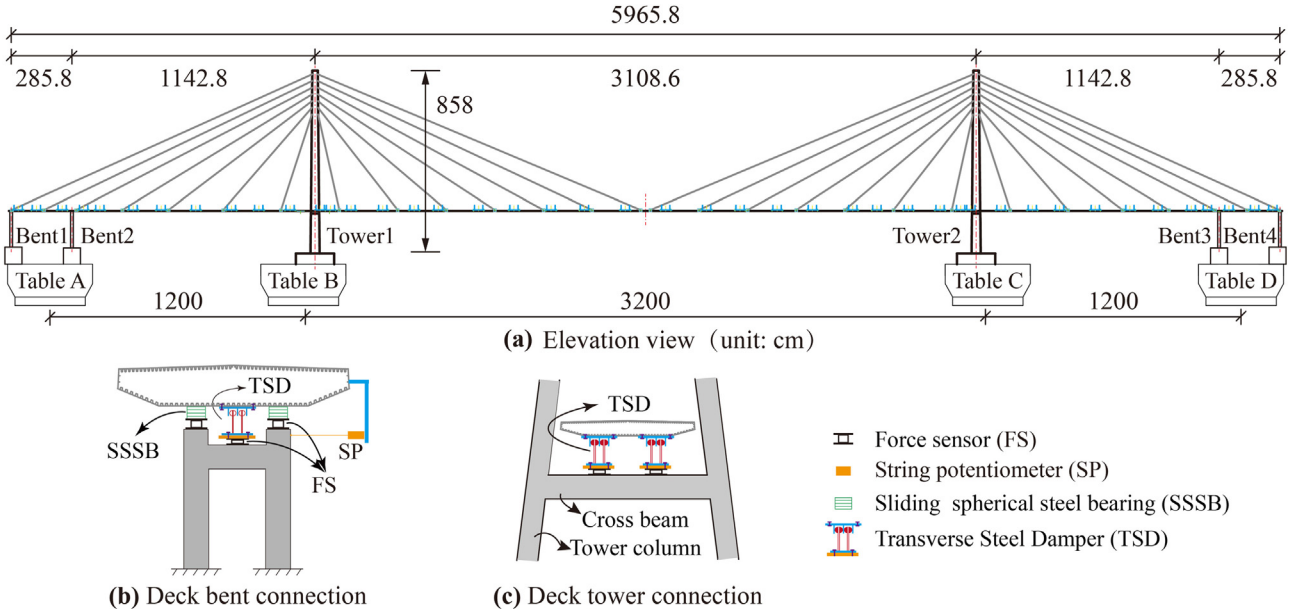

Fig. 1. Layout of the 1–35 scale model and illustration of deck-bent/tower connections.

ground motions with a damping ratio of 3%, together with the first transverse period of the test model bridge equipped TSDs (i.e., 1.92 s) [18]. As shown in this figure, the values of acceleration response spectra of San Fernando and Landers ground motions near the first transverse period of the test model are obviously greater than that of El Centro and Chi-Chi. Therefore, the first two ground motions can trigger larger displacements of TSDs.

To enhance the verification of fatigue performance of TSDs under different ground motion sequences, two quite different synthetic ground motion sequences are adopted as excitations. The ground motion sequence S1 shown in Fig. 8 consists of 0.5 g Landers (repeated five times), 0.3 g San Fernando (repeated three times) and 0.5 g San Fernando (repeated three times), which can compel the TSD experience quite large displacement amplitudes. The ground motion sequence S2 shown in Fig. 9 is orderly comprised of 0.5 g El Centro, 0.5 g Chi-Chi, and San Fernando (gradually increased PGA) ground motions, which can compel the TSD experience the displacements with a gradually increasing trend in general. As aforementioned, two types of TSD (named TSD-1 and TSD-2) are tested, which are installed in the bridge model separately. The sequences S1 and S2 were adopted as the excitation for the case with TSD-1 and TSD-2, respectively. It is worth

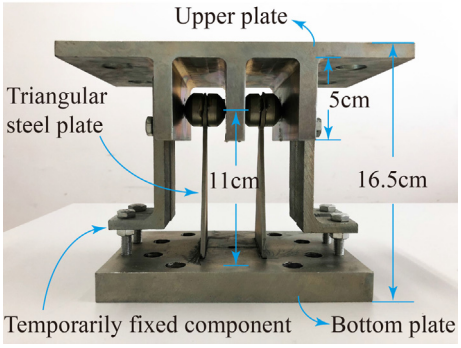

Fig. 3. Configuration of the tested TSD.

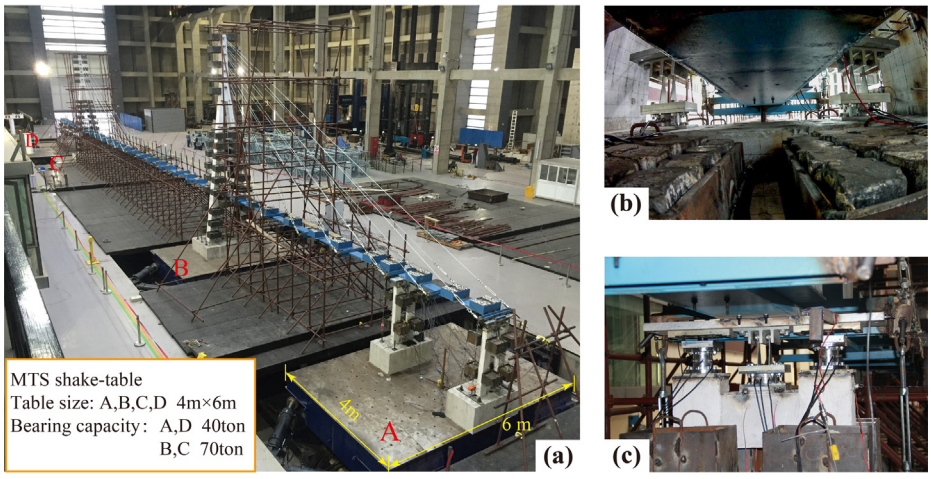

Fig. 2. Photos for shake table test: (a) full view of the test model, (b) Deck-Tower 1 connection, and (c) Deck-Bent 2 connection.

Table 1
Geometric parameters and configuration of two types of tested TSD.

	Height/cm	Width/cm	Thickness/cm	Number of triangular plates	Yield strength of steel for triangular plates/MPa
TSD-1	11	7	0.3	2	326
TSD-2	11	7	0.3	2	193

noting that the purpose of using different ground motion sequences for different sets of TSDs is to form a wide range of cases as far as possible.

3. Test results

3.1. Displacement response and hysteretic behavior of TSDs

Fig. 10 presents seismic responses of TSD-1 under the ground motion sequence S1. Fig. 10(a) shows displacement time-histories of TSD under each ground motion, together with the peak maximum/minimum displacements and the residual ones. It is clear that a gradually increasing trend is observed in the residual displacements. In addition, the pulse-like Landers ground motion triggers obvious displacement pulses, which results in less hysteretic cycles as shown in Fig. 10(b). By contrast, the TSD undergoes more hysteretic cycles with large deformations under the non-pulse-like San Fernando ground motion, since it contains more low-frequency components than other three ground motions. More importantly, as presented in Fig. 10(c), stable and nearly coincident hysteretic curves of TSD-1 under the last two shakings (S1–10 and S1–11) are recorded, which preliminarily indicates that no fatigue failure occurs in the TSD-1. In addition, the plump hysteretic curves represent the excellent energy dissipation capacity of TSDs.

Fig. 11 shows seismic responses of TSD-2 under the ground motion sequence S2. The peak displacements and residual displacements of TSD under S2 are also presented in Fig. 11(a). Similar to the above results, residual displacements with an increasing trend are observed. In addition, stable and nearly coincident hysteretic curves are recorded under the last two shakings (S2–12 and S2–13), which also indicates that no fatigue failure occurs in TSD-2.

Fig. 12 quantifies the dissipated energy of TSD-1 and TSD-2 under each ground motion. The energy is calculated as the total area of the force-displacement hysteretic loops. Considerable differences on the dissipated energy are detected among El Centro, Chi-Chi, Landers and Fernando ground motions, although they have an identical PGA of 0.5 g. This result indicates that PGA is not an optimal intensity measure for predicting the energy dissipation of TSDs under earthquakes. Further studies are required to assess effects of other characteristics of ground motions and dynamic properties of structures on energy dissipation properties of TSDs.

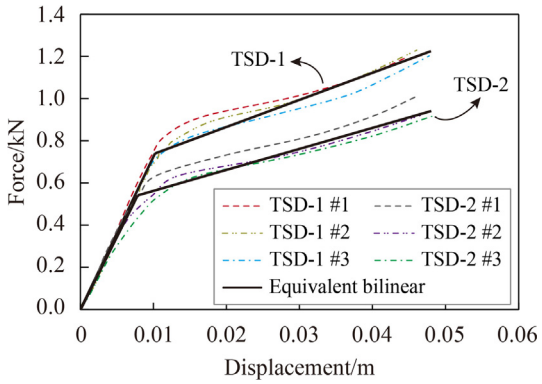

Fig. 5. Force-displacement relationship of TSDs.

Table 2
Mechanical parameters of TSDs.

	Yield strength, kN	Pre-yield stiffness, kN/m	Post-yield stiffness, kN/m
TSD-1	0.74	73	13.5
TSD-2	0.54	69	10.7

Table 3
Information of the adopted PEER-NGA ground motion records.

#	Earthquake, Year	Station	RSN	V_{s30} (m/s)	M_w	R (km)
1	San Fernando, 1971	LB-Terminal Island	69	217.92	6.61	58.99
2	Imperial Valley-02, 1940	El Centro	6	213.44	6.95	6.09
3	Chi-Chi, 1999	TCU129	1549	511.18	7.62	1.83
4	Landers, 1992	Lucerne	879	1369.0	7.28	2.19

3.2. post-earthquake observation of TSDs

Fig. 13 shows the post-shaking deformation of TSDs at different connections after experiencing the sequences S1 and S2. Due to the symmetry of structure, only TSDs at deck-Bent 1, deck-Bent 2, and deck-Tower 1 connections are presented. Except for the observed

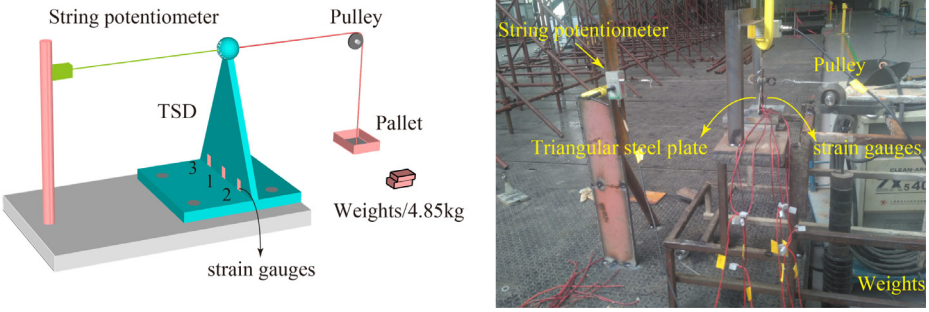

(a) Illustration for the load system (b) Photo of the quasi-static test

Fig. 4. Load scheme and device in quasi-static tests for TSD.

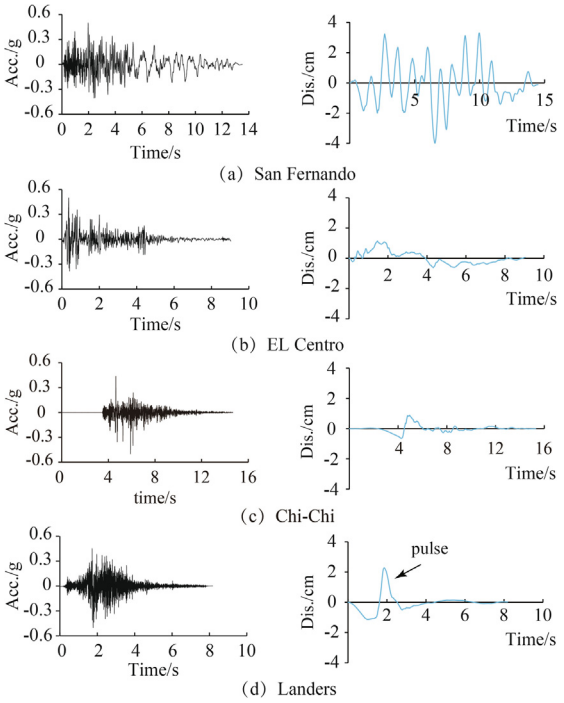

Fig. 6. Time compressed ground motions with a PGA of 0.5 g.

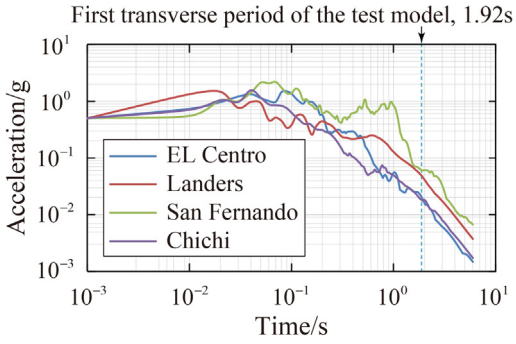

Fig. 7. Acceleration response spectra (3% damping ratio) of the time-compressed ground motions with PGA = 0.5 g.

residual deformations, no other physical damages such as fracture or crack were observed in the tested TSDs. As seen in Fig. 13, almost the same residual deformation was captured for the two pieces of triangular steel plates in a TSD at deck-Tower1 connections after shaking. The observed slight difference of the residual deformation for the two pieces of steel plates in the TSD at deck-Bent 2 (marked in bold) may owe to: (1) variation in steel yield-strength results in the strength difference between the two pieces of triangular steel plates; and (2) a slight manufacturing error in the size of triangular steel plates and hemisphere at the top of plate. In addition, load paths from the deck to bents/towers were never interrupted during the tests, which also implies that the TSDs reserved their full functions during shakings.

3.3. Post-earthquake capacity of TSDs

To further inspect the potential damage state of TSD-1 and TSD-2 after experiencing ground motion sequences and to assess their post-earthquake capacities, monotonic loading tests using the simplified loading device as previously shown in Fig. 4 were performed along the residual deformation direction of TSDs. As shown in Fig. 14, for comparing with the pre-earthquake performance of TSDs, the recorded post-earthquake capacity curves of TSD-1 and TSD-2 are compared with their pre-earthquake capacity curves (previously shown in Fig. 5). As can be seen from these comparisons, no strength or stiffness degradation occurs in the TSDs although they experienced a series of ground motions, which could further indicate that no low cycle fatigue failure occurs in TSDs. By contrast, a slight hardening of post-yield stiffness of TSDs is observed. In addition, the dynamic force-displacement skeleton curves of TSD-1 and TSD-2 obtained from their hysteretic loops under the S1-11 and S2-13 are compared with the pre-earthquake capacity curves. In general, good agreements are achieved, which can validate the reliability of bilinear constitutive models of TSDs. Note that the post-earthquake capacity curves and in-earthquake skeleton curves of TSDs with residual deformation are also shown in the gray region of each subfigure as a supplement. The residual deformation of TSD under each ground motion are marked in Figs. 10(a) and 11(a).

4. Assessments on the low cycle fatigue performance of TSDs

4.1. Assessment using the strain-based method

4.1.1. Introduction of the strain-based method

A strain-based model for the low cycle fatigue life prediction was first proposed by Monson in 1952 [19], which has been extensively calibrated and widely used for steel specimens subjected to constant plastic-strain ranges [14,34,36]. In this model, the fatigue life is directly related to the plastic strain range, as expressed in Eq. (1).

$$N_f = \frac{1}{2}\left[\frac{\Delta\varepsilon_p}{2\varepsilon_f'}\right]^{\frac{1}{c}} \tag{1}$$

where N_f is the fatigue life or the number of load cycles to fatigue failure; $\Delta\varepsilon_p$ is the plastic strain range which is equal to the positive plastic strain amplitude (ε_{p+}) plus the absolute value of negative plastic strain amplitude (ε_{p-}); ε_f' is fatigue ductility coefficient equal to the failure strain for a single reversal; and c is the fatigue ductility exponent.

Actually, structural components will experience non-constant cyclic strains during earthquakes. To evaluate the cumulative damage of these components, a common method using the Miner's rule [37,38] is adopted, which assumes that the cumulative damage (D_c) imposed on the structural component is equal to the linear summation of all damage fractions (D_m), as expressed in Eq. (2).

$$D_c = \sum_{m=1}^{n_t} D_m = \sum_{m=1}^{n_t} \frac{1}{(N_f)_m} \tag{2}$$

where n_t is the total number of cycles during cyclic loading; and $(N_f)_m$ is the fatigue life corresponding to the plastic strain range in the m^{th} cycle. Failure is assumed when D_c exceeds unity (i.e., 1).

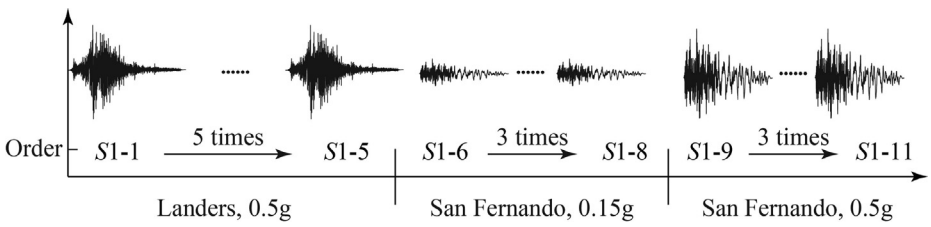

Fig. 8. Ground motion sequence S1 for TSD-1.

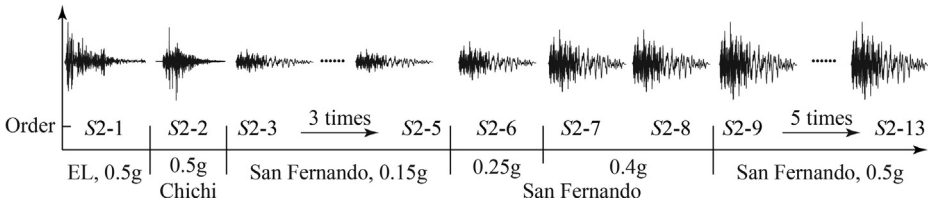

Fig. 9. Ground motion sequence S2 for TSD-2.

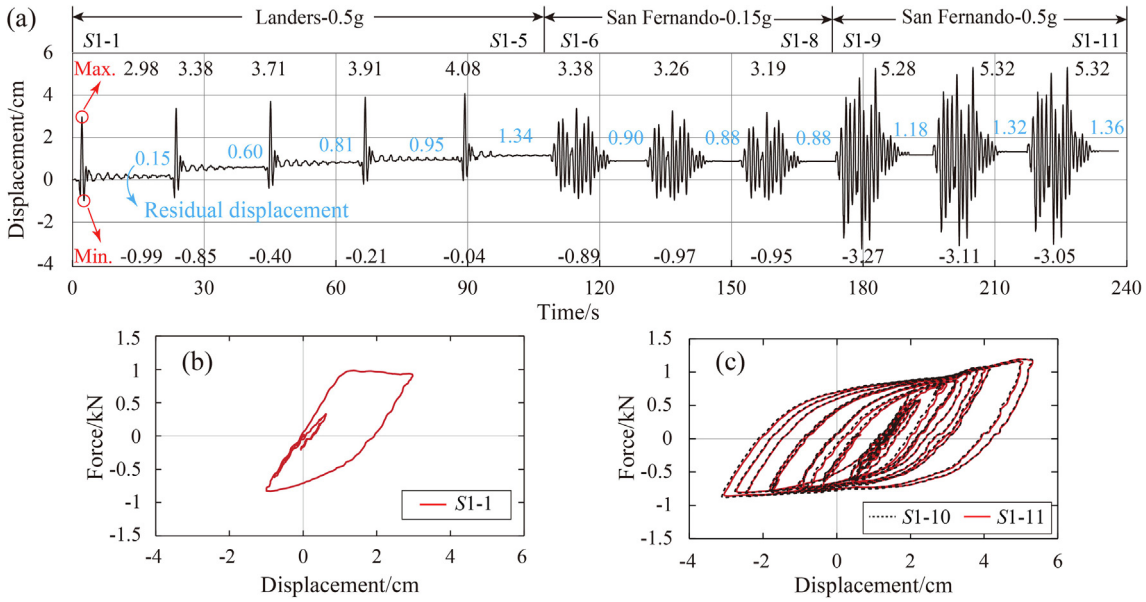

Fig. 10. Seismic responses of TSD-1 under earthquake sequence S1: (a) displacement time-histories; (b) and (c) hysteretic curves of TSD-1 under Landers (S1-1) and San Fernando (S1-10 and S1-11), respectively.

4.1.2. Improvements for the strain-based method

In engineering applications, however, the evaluation of damage or fatigue life through plastic strains is less convenient as compared to that through plastic displacements, because displacement responses rather than strains are much easier to obtain. In this regard, Eq. (3) is adopted to estimate the strain at the bottom of a triangular steel plate. Once the displacement demands of the triangular steel plate are obtained, the low cycle fatigue performance can be then evaluated using Eqs. (1) and (2), as adopted in [34].

$$\varepsilon(t) = \frac{u(t) \times t_p}{H_p^2} \tag{3}$$

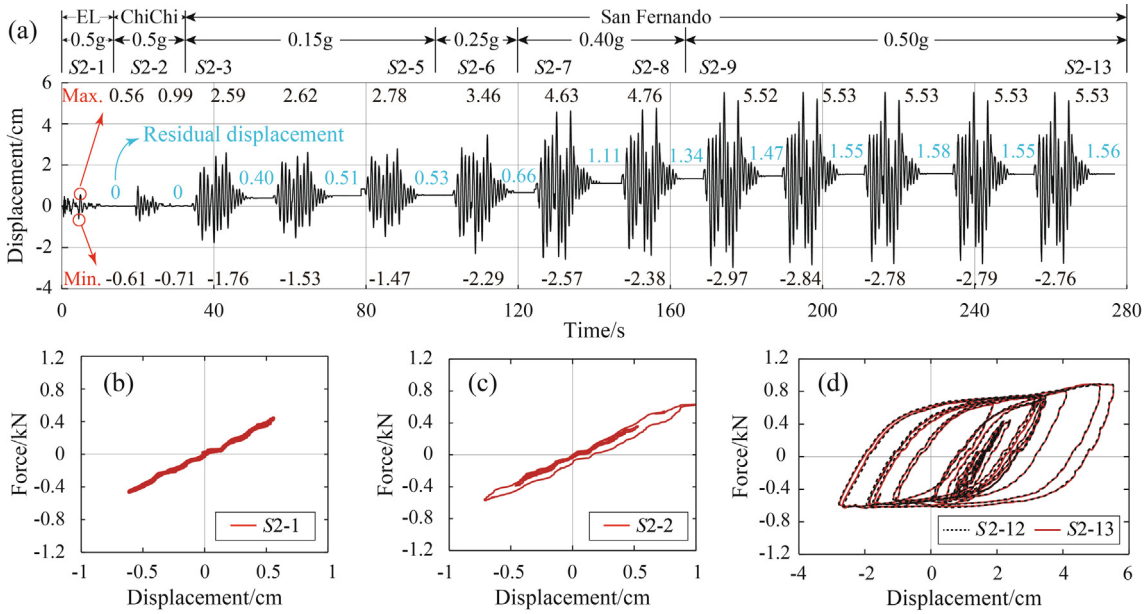

Fig. 11. Seismic responses of TSD-2 under earthquake sequence S2: (a) displacement time-histories; (b), (c), and (d) hysteretic curves of TSD-2 under El Centro (S2-1), Chi-Chi (S2-2), and San Fernando (S2-12, S2-13), respectively.

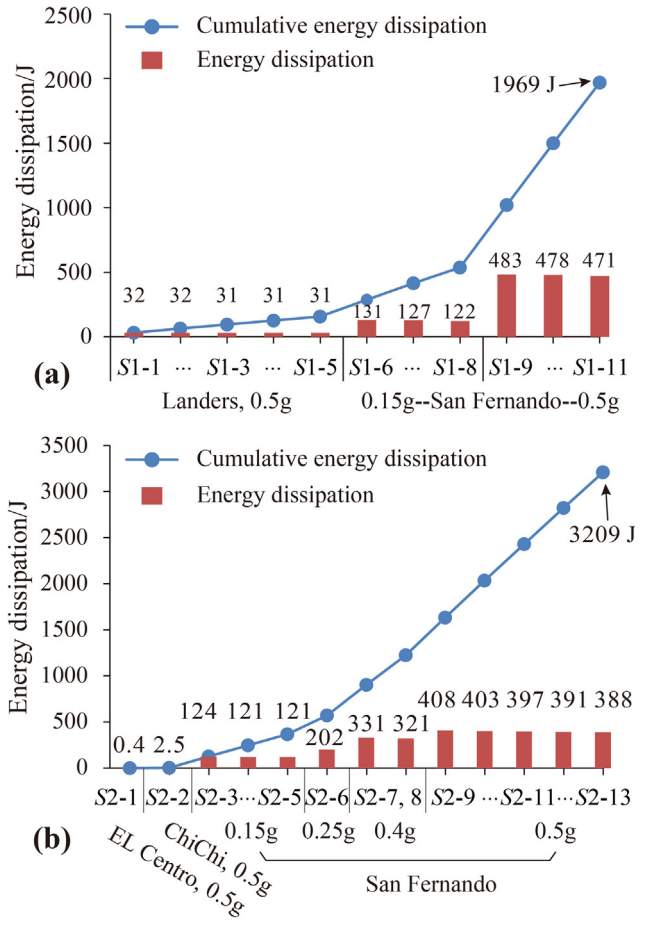

Fig. 12. Energy dissipation of TSDs under earthquake sequences: (a) TSD-1, and (b) TSD-2.

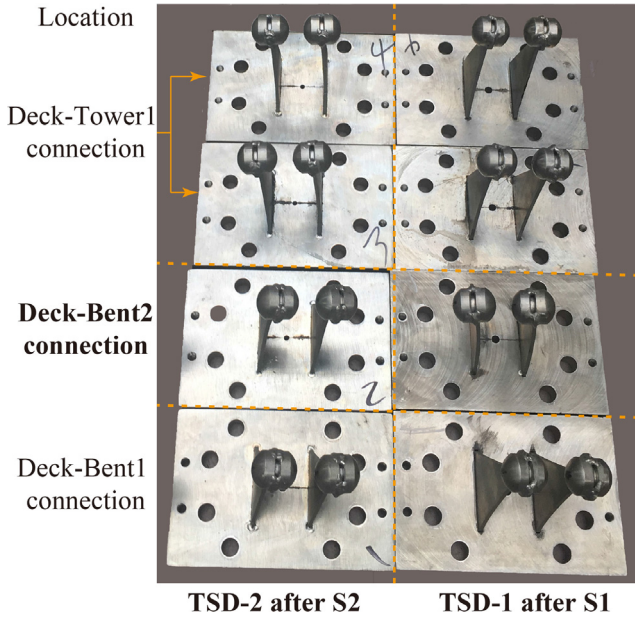

Fig. 13. Deformation mode of TSDs after experiencing the ground motion sequences S1 and S2.

where $\varepsilon(t)$ is a plate-bottom strain at t time; $u(t)$ is the horizontal displacement of plate-top at t time; t_p and H_p is thickness and height of a plate, respectively.

However, Eq. (3) can merely be applied in the cases when the steel is in the elastic state, while for TSDs undergoing apparently inelastic deformations, the strain-displacement relationships should be nonlinear and there were no mathematical formations for such nonlinear relationships. Therefore, it is very necessary to establish such relationships. In general, the numerical fitting is a feasible way for establishing the relationship between the strain and displacement, which can be expressed in a uniform formula as shown in Eq. (4). The plastic strain range of TSD within any n^{th} cycle can then be calculated by the displacement amplitude as shown in Eq. (5), which is derived from the definition of plastic strain range. A practical prediction model of low cycle fatigue is subsequently developed as expressed in Eq. (6).

$$\varepsilon(t) = f(u(t)) \tag{4}$$

$$(\Delta\varepsilon_p)_n = f(u_n^a) = \begin{cases} f(|u_n^+|) + f(|u_n^-|) - 2\varepsilon_y, & |u_n^+|,\ |u_n^-| > u_y \text{ and } u_n^+ \cdot u_n^- < 0 \\ |f(|u_n^+|) - f(|u_n^-|)|, & |u_n^+|,\ |u_n^-| > u_y \text{ and } u_n^+ \cdot u_n^- > 0 \\ f(\max(|u_n^+|, |u_n^-|)) - \varepsilon_y, & |u_n^+| \text{ or } |u_n^-| > u_y \\ 0, & |u_n^+| \text{ and } |u_n^-| \leqslant u_y \end{cases} \tag{5}$$

$$N_f = \frac{1}{2}\left[\frac{f(u_n^a)}{2\varepsilon_f'}\right]^{\frac{1}{c}} \tag{6}$$

where $(\Delta\varepsilon_p)_n$ and u_n^a are the plastic strain range and displacement amplitude in the n^{th} cycle, respectively; u_n^+ and u_n^- are the displacement in the crest and trough of n^{th} cycle, respectively; ε_y is the yield strain of steel; and u_y is the displacement at plate-top corresponding to the steel yield-strain, which can be calculated by Eq. (7) for the triangular plate.

$$u_y = \frac{\varepsilon_y \times H_p^2}{t_p} \tag{7}$$

4.1.3. Assessment procedures and results

As mentioned in Section 4.1.2, the relationship between the strain at the bottom of a triangular steel plate and the displacement at its vertex should be established at first before assessing the low cycle fatigue performance of TSDs. These two data can be obtained by numerical analyses using ABAQUS [39], and then the strain-displacement relationship can be determined by the numerical fitting.

Taking the two types of TSDs in this study as examples, their three-dimensional finite element models are established using ABAQUS software, as indicatively illustrated in Fig. 15. In these numerical models, the plate is modeled using the shell element. A displacement-controlled monotonically lateral loading pattern is applied at plate-top, and the plate bottom is fixed. A bilinear stress-strain constitutive for metal material is adopted. For the TSD-1, the measured yield strength and Young's modulus are 326 MPa and 205,000 MPa, respectively, while those are 193 MPa and 222,950 MPa for the TSD-2. For both types of materials, the ultimate strain and harden ratio are 0.15 and 0.00423, respectively.

To validate the numerical models in ABAQUS, Figs. 16 and 17 present comparisons between numerical and quasi-static-test results of TSD-1 in terms of global force-displacement curves and local strain-displacement curves. Note that the displacements represent the responses at the vertex of the triangular plate while the strain represents the responses at the midpoint of plate bottom. In general, good agreements between the numerical and experimental results are achieved from a quick view of these two figures, which validates the ABAQUS numerical models.

Based on the validated numerical models in ABAQUS, Fig. 18 shows the strain-displacement relationships of TSD-1 and TSD-2 determined by the numerical fitting. It is clear that the strain responses are obviously underestimated by Eq. (3) especially in the plastic deformation stages, which consequently overestimates the fatigue life of TSDs

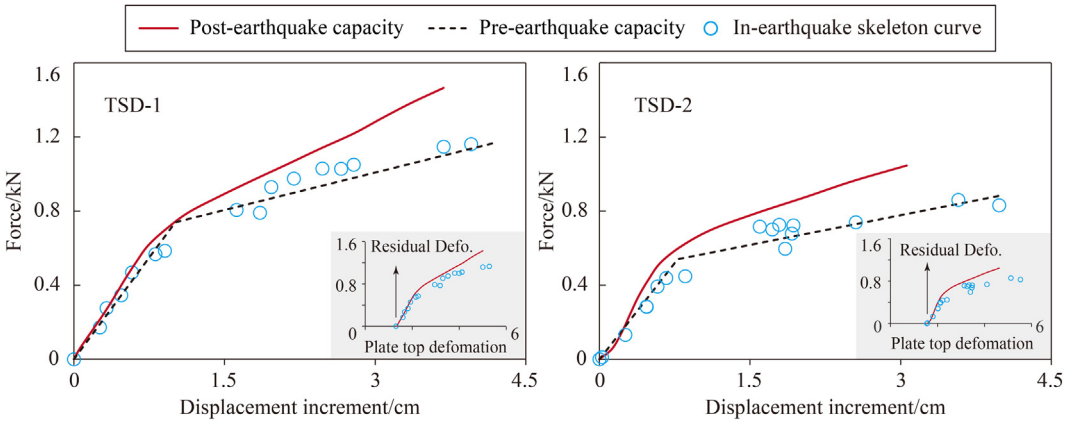

Fig. 14. Skeleton curves of the TSDs at different states.

according to Eq. (1).

Once the strain-displacement relationships are obtained, the low cycle fatigue performance of TSDs can be assessed using Eqs. (5) and (6) as well as Eq. (2). As shown in Eq. (6), the decrease of c and ε_f' will result in a decrease of fatigue life N_f, which leads to an increase of cumulative damage index, D_c. For most metals, the value of exponent c varies between -0.5 and -0.8, and an average value of $c = -0.6$ is commonly assumed for steel [36]. Note that Manson [40], Camara [34], Mander [41], and Ou [42] recommended c values of -0.6, -0.55, -0.486, and -0.4112, respectively, which are adopted in this study. In addition, the value of ε_f' is also directly related to the properties of steel materials. In this paper, ε_f' is conservatively taken as 0.15 [43–45].

Combined with the measured displacement time-histories of TSD-1 and TSD-2 and the established strain-displacement formulas shown in Fig. 18, the cumulative damage indexes of the two types of TSDs under ground motion sequences S1 and S2 can be calculated, respectively, using Eqs. (5), (6) and (2). Table 4 lists the cumulative damage index D_c of TSD-1 and TSD-2 corresponding to different c values. In general, the D_c values of TSD-1 and TSD-2 are less than unity, which indicates that no fatigue failure occurs in TSD-1 and TSD-2 though they experienced 11 and 13 times strong shakings, respectively. This conclusion can also be validated by three reliable proofs presented in Section 3, namely (1) For the tested TSDs, no other physical damage except residual deformation was observed at the end of tests; (2) The stable and nearly coincident hysteretic curves of TSDs under last two loadings are observed; (3) No strength or stiffness degradation occurs in the post-earthquake capacity curves of TSD-1 and TSD-2.

In addition, as can be seen from Table 4, the unimproved method (using Eqs. (3), (1) and (2)) obviously underestimate the damage index

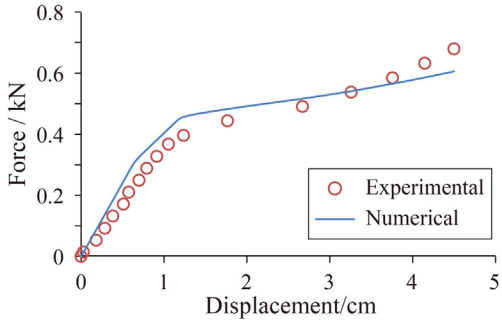

Fig. 16. Force-displacement curves at the plate top (TSD-1).

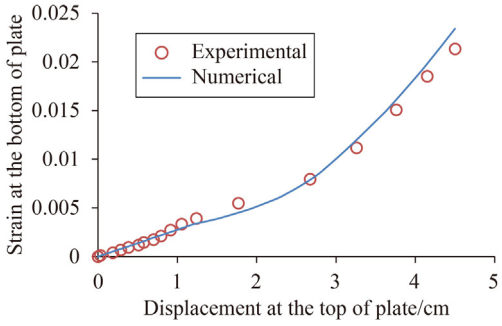

Fig. 17. Strain-displacement curves at the plate-bottom-midpoint of TSD-1.

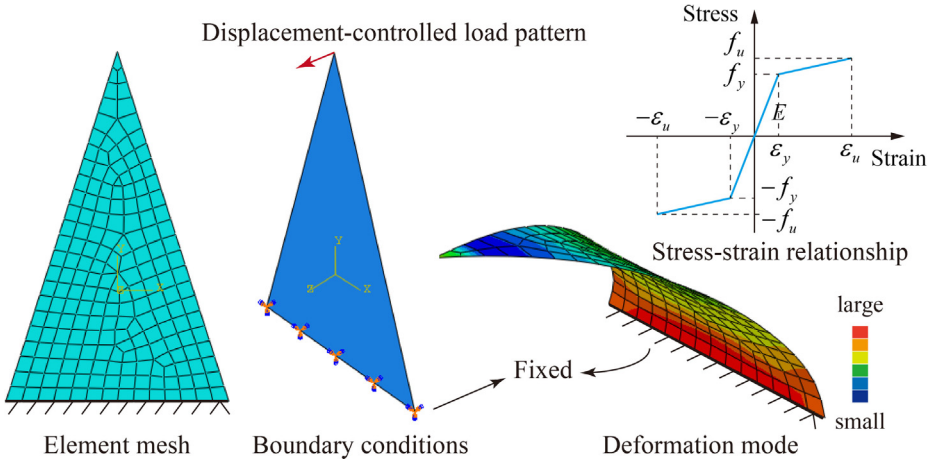

Fig. 15. Finite element model of TSD.

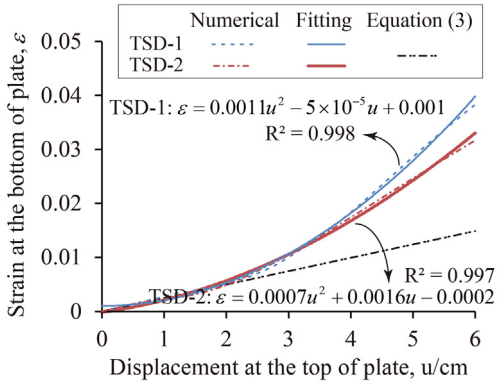

Fig. 18. Strain-displacement relationships of TSDs.

D_c resulting in a perilous evaluation of low cycle fatigue performance, which is caused by the obviously underestimated strain response using Eq. (3) as shown in Fig. 18.

4.2. Assessment using cumulative inelastic deformation

The cumulative inelastic deformation (CID) is another widely used method to describe the plastic capacity of the metallic dampers, which is defined as Eq. (8) [46].

$$CID = \sum_{m=1}^{n_t} \Delta\varepsilon_{tp}^{m} \tag{8}$$

where n_t is the total number of loading cycles of a specimen with plastic deformation. $\Delta\varepsilon_{tp}^{m}$ is a total plastic strain in the m^{th} cycle, which is the summation of positive plastic strain amplitude (ε_{p+}) and the absolute value of negative plastic strain amplitude (ε_{p-}).

Table 5 lists the TSD-experienced inelastic deformation and hysteretic cycles. As can be seen from these results, the maximal strain ε_{max} of both TSDs is up to 3%, and the CID values of TSD-1 and TSD-2 are far larger than 0.7, which is a threshold of high-performance seismic dampers proposed by Usami [47]. Moreover, these CID values are far larger than $200\varepsilon_y$ (0.318 for TSD-1 and 0.173 for TSD-2), which is a threshold of low cycle fatigue performance for BRBs stipulated by AISC [28]. Where ε_y is the yield strain of metal material, which is 0.00159 and 0.000866 for TSD-1 and TSD-2, respectively. These assessment results indicate that TSDs possess good fatigue performance. Table 5 also summarizes the cumulative hysteretic cycles of TSDs under different plastic strain ranges $\Delta\varepsilon_p$. The $n_{\Delta\varepsilon_p \geqslant 8\varepsilon_y}$ and $n_{\Delta\varepsilon_p \geqslant 16\varepsilon_y}$ represent the hysteretic cycles of TSDs when the plastic strain ranges are not less than $8\varepsilon_y$ and $16\varepsilon_y$, respectively.

4.3. Assessment using equivalent hysteresis cycles

In Chinese specification [29], the metallic hysteretic dampers shall withstand more than 30 hysteretic cycles under design displacements. Due to the fact that dampers are usually subjected to non-constant displacement amplitudes under earthquakes, the equivalent hysteretic cycles (EHCs) is proposed in this study based on the principle of equal energy dissipation, as expressed in Eq. (9).

$$EHCs = \frac{CED}{E_d} \tag{9}$$

where CED is cumulative energy dissipation of dampers under earthquakes; and E_d is energy dissipation capacity of dampers corresponding to its design displacement u_d, which is illustrated in Fig. 19. Two main principles are taken into consideration when determining the design displacement of TSD. One is to retain the integrity of the TSD, namely preventing the hemispheres from jumping out of the steel blocks. The other is that the strain at the bottom of the triangular steel plate corresponding to the design displacement should be less than its ultimate strain.

Combined with the mechanical parameters of TSDs listed in Table 2, the energy dissipation quantity of TSD-1 and TSD-2 corresponding to their design displacement (both are 4.7 cm) is 88.9 J and 71.5 J, respectively. As presented in Fig. 12, the cumulative energy dissipation quantity of TSD-1 under ground motion sequence S1 and TSD-2 under S2 is 1969 J and 3209 J, respectively. Using the definition of EHCs described in Eq. (9), the EHCs of TSD-2 under ground motion sequences S2 is around 45 cycles, which is far larger than 30 cycles as stipulated in the Chinese specification [29]. Due to the imperfection of loading scheme for TSD-1, the EHCs of 22 for TSD-1 is less than 30. Nonetheless, the CID is far larger than 0.7 and $200\varepsilon_y$ as presented above. In addition, it is worth noting that the EHCs of TSD-1 and TSD-2 corresponding to fatigue-failure-state may be larger since these values are calculated before the occurrence of fatigue failure in TSDs. Therefore, the experimental results could reasonably conclude that TSDs possess an excellent low cycle fatigue performance.

Table 5
Cumulative inelastic deformation and hysteretic cycles of TSDs.

Test specimen	n_t	$n_{\Delta\varepsilon_p \geqslant 8\varepsilon_y}$	$n_{\Delta\varepsilon_p \geqslant 16\varepsilon_y}$	ε_{max}	CID
TSD-1	110	27	6	0.032	1.732
TSD-2	173	85	48	0.030	3.279

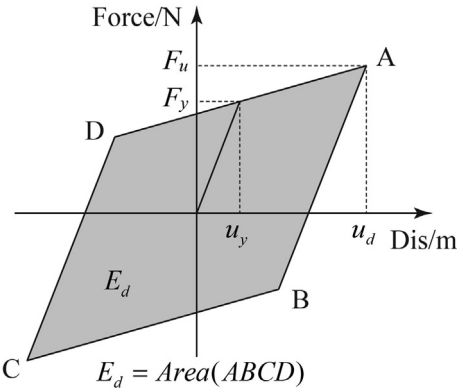

Fig. 19. Energy dissipation capacity of TSD.

Table 4
Damage index D_c of TSDs in different c values.

Specimen	method	c value			
		−0.4112 [42]	−0.486 [41]	−0.55 [34]	−0.60 [40]
TSD-1	Improved method	0.103	0.274	0.525	0.799
	Unimproved method	0.022	0.079	0.184	0.315
TSD-2	Improved method	0.177	0.495	0.970	1.495
	Unimproved method	0.052	0.183	0.413	0.695

5. Conclusions

This paper aims to examine the low cycle fatigue performance of TSDs using shake-table tests. Two sets of TSDs with different yield-strengths are installed separately on a 1/35-scaled cable-stayed bridge model, which is subjected to ground motion sequences in a four-shake-table system. After that, the post-earthquake capacities of TSDs were further examined using monotonic quasi-static tests. Then three different methods including improved strain-based method, cumulative inelastic deformation (CID) and equivalent hysteretic cycles (EHCs) are used to assess the fatigue performance of TSDs. The main remarkable findings and conclusions are summarized as follows:

(1) No fatigue failure occurred in the tested TSDs even though they experienced more than ten seismic excitations.
(2) The results obtained from the three theoretical assessment methods indicate that TSDs possess an excellent low cycle fatigue performance.
(3) It is practical for the improved strain-based damage assessment framework. The low-cycle fatigue assessment methods summarized in this paper can be applied in other types of metallic hysteretic dampers.

Acknowledgements

This work is supported by the National Basic Research Program of China (No. 2013CB036302) and National Natural Science Foundation of China (Grant 51778469). All staffs in the Multi-Functional Shaking Table Lab of Tongji University are greatly acknowledged, especially Drs. Jianzhong Li, Zhongguo Guan and Yan Xu who provided lots of insightful suggestions to the test. The authors also acknowledge the anonymous reviewers who have contributed to essentially improving the paper.

References

[1] Weber F, Feltrin G, Huth O. Guidelines for structural control. Struct Eng Res Lab Swiss Fed Lab Mater Test Res Dubendorf, Switz 2006:155.
[2] Jun Guo J, Zhong J, Zhi Dang X, Cheng Yuan W. Seismic performance assessment of a curved bridge equipped with a new type spring restrainer. Eng Struct 2017. doi:10.1016/j.engstruct.2017.08.006.
[3] Wei B, Wang P, Yang M, Jiang L. Seismic response of rolling isolation systems with concave friction distribution. J Earthq Eng 2017. https://doi.org/10.1080/13632469.2016.1157530.
[4] Wang X, Fang J, Zhou L, Ye A. Transverse seismic failure mechanism and ductility of reinforced concrete pylon for long span cable-stayed bridges: Model test and numerical analysis. Eng Struct 2019. https://doi.org/10.1016/j.engstruct.2019.03.045.
[5] Kasai K, Fu Y, Watanabe A. Passive control systems for seismic damage mitigation. J Struct Eng 1998;124:501–12. https://doi.org/10.1061/(ASCE)0733-9445(1998)124:5(501).
[6] Vulcano A, Mazza F. Comparative study of the seismic performance of frames using different dissipative braces. Proc 12th world conf earthq eng. 2000. p. 1–8.
[7] Chen X, Ge H, Usami T. Seismic demand of buckling-restrained braces installed in steel arch bridges under repeated earthquakes. J Earthq Tsunami 2011;05:119–50. https://doi.org/10.1142/S1793431111000942.
[8] Kelly JM, Skinner RI, Heine AJ. Mechanisms of energy absorption in special devices for use in earthquake resistant structures. Bull New Zeal Soc Earthq Eng 1972;5:63–73.
[9] Skinner RI, Tyler RG, Heine aJ, Robinson WH. Hysteretic dampers for the protection of structures from earthquakes. Bull New Zeal Natl Soc Earthq Eng 1980;13:22–36.
[10] Whittaker AS, Bertero VV, Thompson CL, Alonso LJ. Seismic testing of steel plate energy dissipation devices. Earthq Spectra 1991;7:563–604. https://doi.org/10.1193/1.1585644.
[11] Tsai Keh-Chyuan, Chen Huan-Wei, Hong Ching-Ping, Yung-Feng Su. Design of steel triangular plate energy absorbers for seismic-resistant construction. Earthq Spectra 1993;9:505–28. https://doi.org/10.1193/1.1585727.
[12] Camara A, Astiz MA. Analysis and control of cable-stayed bridges subject to seismic action. Struct Eng Int J Int Assoc Bridg Struct Eng 2014;24:27–36. https://doi.org/10.2749/101686614X13830790993762.
[13] Shen X, Camara A, Ye A. Effects of seismic devices on transverse responses of piers in the Sutong Bridge. Earthq Eng Eng Vib 2015;14:611–23. https://doi.org/10.1007/s11803-015-0049-7.
[14] Usami T, Wang CL, Funayama J. Developing high-performance aluminum alloy buckling-restrained braces based on series of low-cycle fatigue tests. Earthq Eng Struct Dyn 2012;41:643–61. https://doi.org/10.1002/eqe.1149.
[15] Tanaka K, Sasaki Y. Hysteretic performance of shear panel dampers of ultra low yield-strength steel for seismic response control of buildings; 2000. p. 1–8.
[16] Skinner RI, Kelly JM, Heine AJ. Hysteretic dampers for earthquake-resistant structures. Earthq Eng Struct Dyn 1974;3:287–96. https://doi.org/10.1002/eqe.4290030307.
[17] Shen X, Wang X, Ye Q, Ye A. Seismic performance of transverse steel damper seismic system for long span bridges. Eng Struct 2017;141:14–28. https://doi.org/10.1016/j.engstruct.2017.03.014.
[18] Zhou L, Wang X, Ye A. Shake table test on transverse steel damper seismic system for long span cable-stayed bridges. Eng Struct 2019. https://doi.org/10.1016/j.engstruct.2018.10.073.
[19] Manson SS. Fatigue: a complex subject-some simple approximations. Exp Mech 1965;5:193–226. https://doi.org/10.1007/BF02321056.
[20] Ne D. Fatigue failure predictions for complicated stress-strain histories. J Mater 1972;7:71–87. doi:1971.
[21] Fuchs HO, Stephens RI, Saunders H. Metal fatigue in engineering (1980). J Eng Mater Technol 1981;103:346. https://doi.org/10.1115/1.3225026.
[22] Farfan S. High cycle fatigue, low cycle fatigue and failure modes of a carburized steel. Int J Fatigue 2004;26:673–8. https://doi.org/10.1016/j.ijfatigue.2003.08.022.
[23] Usami T, Wang C, Funayama J. Low-cycle fatigue tests of a type of buckling restrained braces. Proc Eng 2011;14:956–64. https://doi.org/10.1016/j.proeng.2011.07.120.
[24] Rinaldin G, Amadio C, Fragiacomo M. Effects of seismic sequences on structures with hysteretic or damped dissipative behaviour. Soil Dyn Earthq Eng 2017;97:205–15. https://doi.org/10.1016/j.soildyn.2017.03.023.
[25] Chen H, Xie Q, Li Z, Xue W, Liu K. Seismic damage to structures in the 2015 nepal earthquake sequences. J Earthq Eng 2017;21:551–78. https://doi.org/10.1080/13632469.2016.1185055.
[26] Kato A, Nakamura K, Hiyama Y. The 2016 Kumamoto earthquake sequence. Proc Japan Acad Ser B 2016;92:358–71. https://doi.org/10.2183/pjab.92.359.
[27] Uchide T, Horikawa H, Nakai M, Matsushita R, Shigematsu N, Ando R, et al. The 2016 Kumamoto-Oita earthquake sequence: aftershock seismicity gap and dynamic triggering in volcanic areas. Earth Planets Sp 2016;68:180. https://doi.org/10.1186/s40623-016-0556-4.
[28] American Institute of Steel Construction. Seismic provisions for structural steel buildings. Chicago, America; 2010.
[29] Ministry of Housing and Urban Rural Development of Republic of China. Technical specification for seismic energy dissipation of buildings. Beijing, China: China Architecture & Building Press; 2013.
[30] Tateishi K, Chen T, Hanji T. Extremely low cycle fatigue assessment method for unstiffened cantilever steel columns. Doboku Gakkai Ronbunshuu A 2008;64:288–96. https://doi.org/10.2208/jsceja.64.288.
[31] Kang L, Ge H. Predicting ductile crack initiation of steel bridge structures due to extremely low-cycle fatigue using local and non-local models. J Earthq Eng 2013;17:323–49. https://doi.org/10.1080/13632469.2012.746211.
[32] Wang CL, Usami T, Funayama J, Imase F. Low-cycle fatigue testing of extruded aluminium alloy buckling-restrained braces. Eng Struct 2013;46:294–301. https://doi.org/10.1016/j.engstruct.2012.07.016.
[33] Xu LY, Nie X, Fan JS. Cyclic behaviour of low-yield-point steel shear panel dampers. Eng Struct 2016;126:391–404. https://doi.org/10.1016/j.engstruct.2016.08.002.
[34] Camara A, Cristantielli R, Astiz MA, Málaga-Chuquitaype C. Design of hysteretic dampers with optimal ductility for the transverse seismic control of cable-stayed bridges. Earthq Eng Struct Dyn 2017;46:1811–33. https://doi.org/10.1002/eqe.2884.
[35] Ancheta TD, Bozorgnia Y, Chiou BS-J, Stewart JP, Boore DM, Graves RW, et al. NGA-West2 Database: a database of ground motions recorded in shallow crustal earthquakes in active tectonic. 15th. World Conf Earthq Eng 2012:6.
[36] Chai YH, Romstad KM. Correlation between strain-based low-cycle fatigue and energy-based linear damage models. Earthq Spectra 1997;13:191–209. https://doi.org/10.1193/1.1585941.
[37] Miner MA. Cumulative damage in fatigue. Am Soc Mech Eng - J Appl Mech 1945;12:159–64. https://doi.org/10.1007/978-3-642-99854-6_35.
[38] Krawinkler H, Zohrei M. Cumulative damage in steel structures subjected to earthquake ground motions. Comput Struct 1983;16:531–41. https://doi.org/10.1016/0045-7949(83)90193-1.
[39] Börgesson L. ABAQUS. Dev. Geotech Eng 1996;79:565–70. https://doi.org/10.1016/S0165-1250(96)80047-2.
[40] Smith RW, Hirschberg MH, Manson SS. Fatigue behavior of materials under strain cycling in low and intermediate life range. NASA Tech Note 1977:1200–2. https://doi.org/10.1227/01.neu.0000317404.31336.69.
[41] Mander JB, Panthaki FD, Kasalanati A. Low-cycle fatigue behavior of reinforcing steel. J Mater Civ Eng 1994;6:453–68. https://doi.org/10.1061/(ASCE)0899-1561(1994) 6:4(453).
[42] Bin W, Jinping O. Fatigue properties and design criteria of mild steel yielding energy dissipation. J Earthq Eng 1996;4:8–13.
[43] Shi Y, Wang M, Wang Y. Experimental and constitutive model study of structural steel under cyclic loading. J Constr Steel Res 2011;67:1185–97. https://doi.org/10.1016/j.jcsr.2011.02.011.
[44] Chen Y, Sun W, Chan TM. Cyclic stress-strain behavior of structural steel with yieldstrength up to 460 N/mm^2. Front Struct Civ Eng 2014;8:178–86. https://doi.org/10.1007/s11709-014-0245-y.
[45] Xu L, Nie X, Fan J, Tao M, Ding R. Cyclic hardening and softening behavior of the low yield point steel BLY160: experimental response and constitutive modeling. Int J Plast 2016;78:44–63. https://doi.org/10.1016/j.ijplas.2015.10.009.
[46] Wang CL, Usami T, Funayama J. Improving low-cycle fatigue performance of high-performance buckling-restrained braces by toe-finished method. J Earthq Eng 2012;16:1248–68. https://doi.org/10.1080/13632469.2012.703385.
[47] Usami. Developing high-performance damage control seismic dampers. In: 10th symp ductile des method bridg (special lect), JSCE, Tokyo, Japan; 2007. p. 11–22.